

The theory of axial tomography based on the inverse Radon transform for high-aperture soft X-ray microscopy

© K.P. Gaikovich, I.V. Malyshev, D.G. Reunov, N.I. Chkhalo

Institute of Physics of Microstructures, Russian Academy of Sciences,
603950 Nizhny Novgorod, Russia
e-mail: ilya-malyshev@ipmras.ru

Received May 2, 2023

Revised May 2, 2023

Accepted May 2, 2023

For soft X-ray microscopy in the approximation of geometrical optics, a theoretical model for the formation of the received image is constructed — a relationship is found between the image recorded on the detector and the 3D distribution of the sample absorption index using a high-aperture mirror objective (NA_z 0.3) with a focus depth close to the diffraction limit. The solution of the inverse problem of tomography for determining this 3D distribution from the data of measurements in a high-aperture mirror SXR-microscope is obtained.

Keywords: soft x-ray microscopy, inverse problem of microscopy, absorption contrast imaging.

DOI: 10.61011/TP.2023.07.56620.106-23

Introduction

For a detailed study of cells in modern biology and medicine, it is necessary to obtain their image with a nanometer resolution [1]. Optical microscopy operating in visible light does not allow direct examination of the nanostructure of living cells with details less than 200 nm due to diffraction blurring [2]. Various methods of increasing the resolution of optical microscopy, for example, STED microscopy [3], can significantly exceed the diffraction limit and achieve a resolution of tens of nanometers. However, as in the case of classical fluorescence microscopy, the method allows seeing only tinted organelles in isolation from the environment, which makes it difficult to understand the processes taking place in cells.

Electron microscopy has a high spatial resolution, up to nanometers, [4]. However, the studied samples have to be frozen and cut into films with a thickness of 100–500 nm to conduct such studies, i.e. this method is destructive and cannot be used to study living cells [5]. Atomic force and scanning tunneling microscopy allow studying only the surface of the samples.

On the other hand, soft X-ray microscopy (SX microscopy) has been developing for more than thirty years in the spectral region „of the water transparency window“, wavelengths 2.3–4.4 nm [6–10], as well as in the extreme ultraviolet (EUV) region at wavelengths 13.4–13.8 nm [11–15]. The main advantages of this method in the „water window“ are the following:

- a small wavelength in the diffraction limit provides a nanometer spatial resolution;
- the absorption contrast between carbon-containing structures and water, which is natural by an order of magnitude or more, allows samples to be examined without the use of contrasting and/or fluorescent substances;

- relatively high transmittance and practically no scattering of radiation makes it possible to study cells and tissue sections up to 10–15 μm thick in their native, potentially — alive, state;
- sample preparation is significantly simplified compared to existing nanoscopy methods.

1. SX microscope at wavelength 13.84 nm

Figure 1 shows a diagram and a photo of the microscope developed in IPM RAS [16]. It operates as follows. The laser-plasma source (LPS) consists of Nd: Ekspla YAG laser ($\lambda = 1064$ nm, $E_{impulse} = 0.4$ J, duration 5 ns, frequency 10 Hz), whose radiation is focused on an argon gas target *1* in Fig. 1. The pulsed gas target was formed using an electromagnetic valve described in [17]. The optimal gas pressure at the valve inlet is — 3 atm. The bright line of the ArVIII ion is used at the wavelength $\lambda = 13.84$ nm.

An elliptical collector mirror *2* collects the LPS radiation *1* on a sample installed in the subject area of the lens *3*. The collector has the shape of an ellipsoid. After aspherization and local shape correction, its focus spot from the point source was measured and had an FWHM size of less than 30 μm [18], which makes it possible to efficiently collect the source radiation on the sample. The maximum difference in the intensity of illumination of the sample in the field of view 290 × 290 μm was 10% (maximum in the center, minimum at the edges). The holder with the sample is mounted on a piezoceramic slide that provides axial tomography by moving along the optical axis. The image of the sample with a magnification of 46 times is constructed with a two-mirror lens *4* on CMOS back-side illumination detector *6* with 6.5 μm pixel. The aspherical concave lens mirror provides a large non-aberrant field of

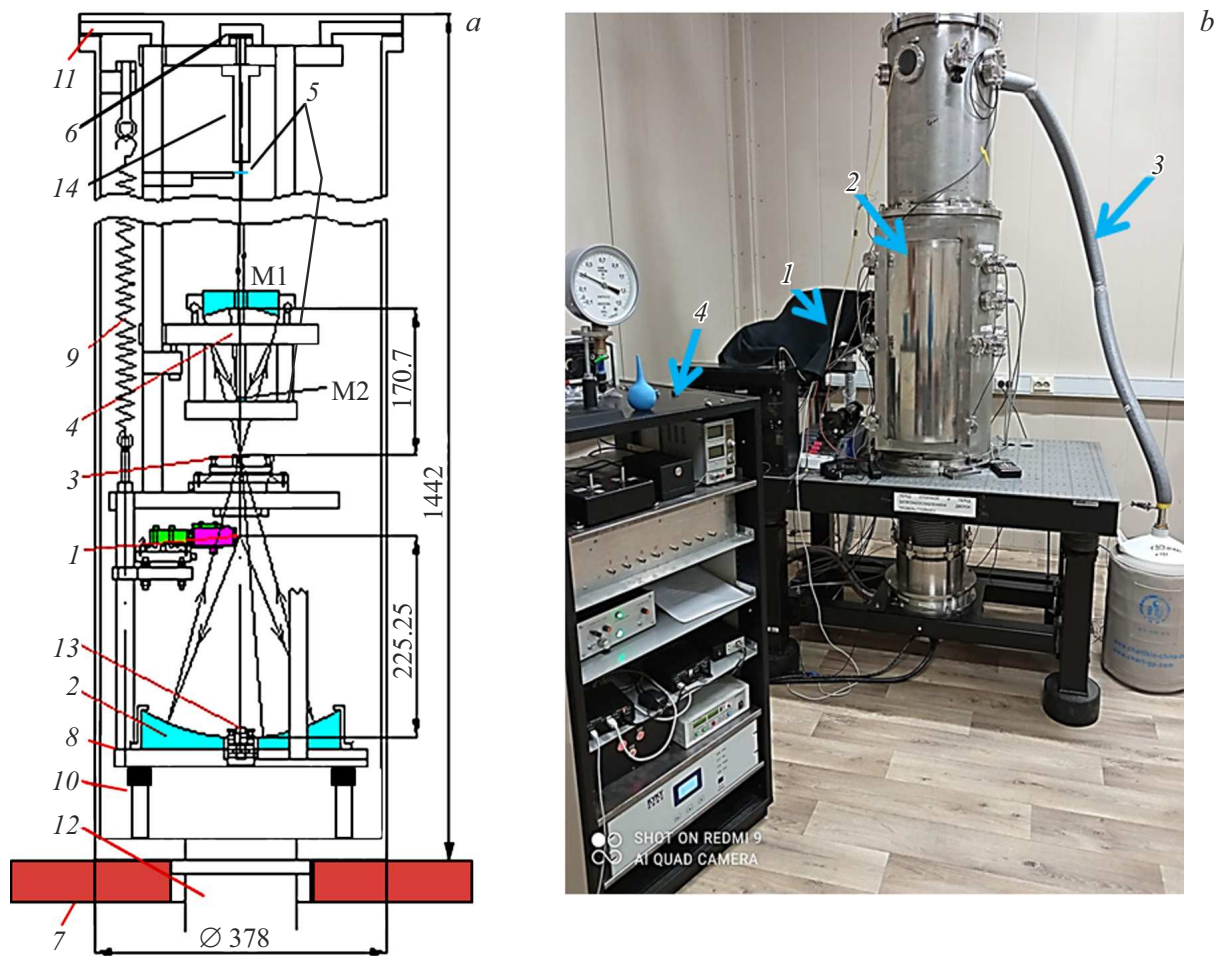


Figure 1. *a* — scheme of a mirror EUV microscope: 1 — laser-plasma source based on pulsed gas target and IR laser, 2 — multilayer elliptical collector mirror, 3 — test sample on 5D-table with the possibility of z -scanning in the vacuum, 4 — a 46-fold dual-mirror lens with a field of view $300 \times 300 \mu\text{m}$ and an aspherical mirror M1, 5 — filters for suppressing long-wave radiation, 6 — CMOS back-side illumination detector, 7 — optical table, 8 — rack with optics, 9 — springs, 10 — supports with rubber inserts, 11 — rack holders, 12 — bellows to turbomolecular pump, 13 — alignment laser; *b* — EUV microscope photograph: 1 — IR laser under the mantle, 2 — vacuum chamber with optics, 3 — detector cooling system, 4 — stand with electronic microscope control systems [16].

view with a size of $290 \times 290 \mu\text{m}$. A Mo/ZrSi₂ 5 filter is installed after the lens to suppress long-wave radiation and transmit 13.84 nm radiation [19]. A series of images is taken at different positions of the sample along the optical axis for subsequent three-dimensional reconstruction of the image.

2. Mathematical model of absorption image reconstruction

2.1. Derivation of the original integral equation from the Radon transformation (direct problem)

The problem of tomography (determining the (3D) distribution of inhomogeneities of the absorption coefficient of the objects under study) is considered in this paper in the approximation of geometric optics, which allows obtaining

the initial equations, which are supposed to be adjusted in the future taking into account diffraction blurring. Figure 2 shows a simplified diagram of the rays in a microscope for a model in which a slight change in their angles within the focus spot inside the cell is neglected.

The signal (intensity) at each point of the measuring matrix is formed by all rays in the cone that have passed through the corresponding focus x_0, y_0, z_0 and exit the camera at points $x_1, y_1, z_1 = 0$ in the measuring chamber (Fig. 1). At the same time, the mirror lens constructs an image of a slice of the sample that has fallen into the focal the plane of the lens ($z = z_0$). For three-dimensional reconstruction of the sample image, it is shifted along the axis z (the optical axis of the lens), and a series of x - y images of the sample is recorded on the camera, the so-called z -stack. The dimension of the scanning grid in the z -plane is determined by the scale of the transverse diffraction

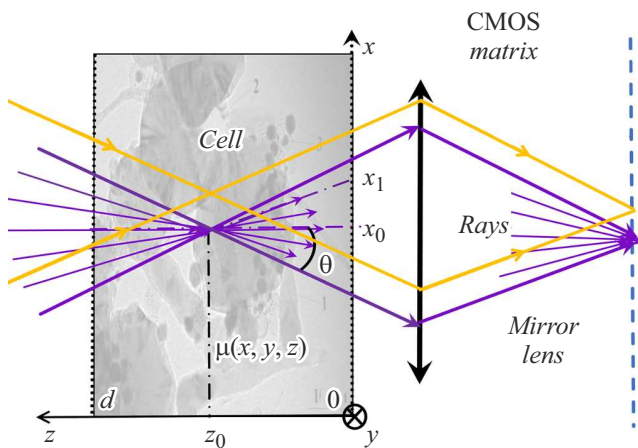


Figure 2. Diagram of the rays of the X-ray microscope in question passing through the sample section located in the focal plane of the lens.

spreading of the radiation in focus. The contribution of each beam to the intensity is determined by the optical absorption thickness — integral along the beam path (Radon transformation) of the absorption coefficient $\mu(x, y, z)$ on a straight line passing through the points x_0, y_0, z_0 and $x_1, y_1, z_1 = 0$ between the planes $z = 0$ and $z = d$:

$$\tau(x_1, y_1, z_1 = 0, x_0, y_0, z_0) = \int_L \mu(x, y, z) dl. \quad (1)$$

The most well-known methods of medical tomography CT (computed tomography) and MRI (magnetic resonance imaging) also lead to a similar equation. These methods are based on the theory of Radon transformations, proposed by him in [20], and later developed for applications in computer X-ray tomography based on the theory of incorrect inverse problems by A.N. Tikhonov with his students [21–24]. In particular, the problem of X-ray tomography in conical beams was considered in [24] in respect to a layered inhomogeneous medium.

The proposed method of tomography of 3D inhomogeneities in this paper is based on solving the inverse problem for the Radon transformation (1) in the geometry of measurements under consideration. We will consider the problem in Cartesian coordinates because unlike CT and MRI there is no cylindrical symmetry in this geometry. We use parametric representation

$$\begin{aligned} \tau(x_1, y_1, z_1, x_0, y_0, z_0) &= \int_{\lambda_1(x_1, y_1, z_1)}^{\lambda_2(x_0, y_0, z_0)} \mu[x(\lambda), y(\lambda), z(\lambda)] \\ &\times \sqrt{[dx(\lambda)/d\lambda]^2 + [dy(\lambda)/d\lambda]^2 + [dz(\lambda)/d\lambda]^2} d\lambda, \end{aligned} \quad (2)$$

of the equation (1) to represent it in these coordinates using the equation for straight lines in 3D:

$$\begin{aligned} x(\lambda) &= x_1 + (x_0 - x_1)\lambda, & y(\lambda) &= y_1 + (y_0 - y_1)\lambda, \\ z(\lambda) &= z_1 + (z_0 - z_1)\lambda. \end{aligned} \quad (3)$$

Then we have

$$\begin{aligned} \tau(x_1, y_1, z_1, x_0, y_0, z_0) &= \sqrt{(x_0 - x_1)^2 + (y_0 - y_1)^2 + (z_0 - z_1)^2} \\ &\times \int_{\lambda_1}^{\lambda_2} \mu[x_1 + (x_0 - x_1)\lambda, y_1 + (y_0 - y_1)\lambda, z_1 + (z_0 - z_1)\lambda] d\lambda \end{aligned} \quad (4)$$

or with integration limits

$$\begin{aligned} \tau(x_1, y_1, z_1, x_0, y_0, z_0) &= \sqrt{(x_0 - x_1)^2 + (y_0 - y_1)^2 + (z_0 - z_1)^2} \\ &\int_{z_1/[z_1+(z_0-z_1)]}^{d/[z_1+(z_0-z_1)]} \mu[x_1 + (x_0 - x_1)\lambda, y_1 + (y_0 - y_1)\lambda, z_1 + (z_0 - z_1)\lambda] d\lambda. \end{aligned} \quad (5)$$

Using the equation of radiation transfer in the absorbing medium, we obtain an expression for the relative (relative to the medium without absorption) intensity at the point x_1, y_1, z_1 for the beam that passed through the focus x_0, y_0, z_0 :

$$\begin{aligned} &\frac{J_0(x_1, y_1, z_1, x_0, y_0, z_0)}{J(x_1, y_1, z_1, x_0, y_0, z_0)[\mu = 0]} \\ &= \exp\left(-\sqrt{(x_0 - x_1)^2 + (y_0 - y_1)^2 + z_0^2}\right. \\ &\left. \times \int_0^{d/z_0} \mu[x_1 + (x_0 - x_1)\lambda, y_1 + (y_0 - y_1)\lambda, z_0\lambda] d\lambda\right). \end{aligned} \quad (6)$$

This expression in Cartesian coordinates is obtained by replacing the variable $z_0\lambda \rightarrow z$:

$$\begin{aligned} &J(x_1, y_1, z_1, x_0, y_0, z_0)/J_0(x_1, y_1, z_1, x_0, y_0, z_0)[\mu = 0] \\ &= \exp\left(-\sqrt{(x_0 - x_1)^2 + (y_0 - y_1)^2 + z_0^2}\right. \\ &\left. / z_0 \int_0^d \mu[x_1 + (x_0 - x_1)z/z_0, y_1 + (y_0 - y_1)z/z_0, z] dz\right). \end{aligned} \quad (7)$$

Further, a solution to the direct problem is obtained — relative intensity at the matrix point corresponding to the

focus position at the point (x_0, y_0, z_0) by integrating over all rays in the cone exiting through the plane $z = 0$:

$$I(x_0, y_0, z_0)/I_0[\mu = 0] = \int_{x_0 - z_0 \operatorname{tg} \theta}^{x_0 + z_0 \operatorname{tg} \theta} dx_1 \int_{-\sqrt{(z_0 \operatorname{tg} \theta)^2 - (x_0 - x_1)^2}}^{\sqrt{(z_0 \operatorname{tg} \theta)^2 - (x_0 - x_1)^2}} dy_1 \exp\left(-\sqrt{(x_0 - x_1)^2 + (y_0 - y_1)^2 + z_0^2} / z_0\right) \times \int_0^d \mu[x_1 + (x_0 - x_1)z/z_0, y_1 + (y_0 - y_1)z/z_0, z] dz \left/ \int_{x_0 - z_0 \operatorname{tg} \theta}^{x_0 + z_0 \operatorname{tg} \theta} dx_1 2\sqrt{(z_0 \operatorname{tg} \theta)^2 - (x_0 - x_1)^2}, \right. \quad (8)$$

where in our case it is possible to use $I_0 = I(\mu = 0) = \text{const}$.

2.2. Solution of the inverse problem of microscopic tomography based on the inverse Radon transformation

An additional condition of smallness of the optical absorption thickness $\tau \ll 1$ is used to solve the inverse tomography problem. Then, the expression

$$\delta I(x_0, y_0, z_0) = [I_0 - I]/I_0 = \iint dx_1 dy_1 \int_{x_0 - z_0 \operatorname{tg} \theta}^{x_0 + z_0 \operatorname{tg} \theta} dx_1 \times \frac{\sqrt{(z_0 \operatorname{tg} \theta)^2 - (x_0 - x_1)^2}}{-\sqrt{(z_0 \operatorname{tg} \theta)^2 - (x_0 - x_1)^2}} dy_1 \sqrt{(x_0 - x_1)^2 + (y_0 - y_1)^2 + z_0^2} / z_0 \times \int_0^d \mu[x_1 + (x_0 - x_1)z/z_0, y_1 + (y_0 - y_1)z/z_0, z] dz, \quad (9)$$

is obtained for a relative decrease in intensity, where the integrand in the integral of z is represented as a double integral of x and y :

$$\delta I(x_0, y_0, z_0) = \iint dx_1 dy_1 \int_0^d \iint dx dy \mu(x, y, z) \times F(x_0 - x_1, y_0 - y_1, z_0) \delta[x - x_1 - (x_0 - x_1)z/z_0] \times \delta[y - y_1 - (y_0 - y_1)z/z_0] dz, \quad (10)$$

and the function

$$F(x_0 - x_1, y_0 - y_1, z_0) = \left\{ \begin{aligned} &= \sqrt{(x_0 - x_1)^2 + (y_0 - y_1)^2 + z_0^2} / \left(2z_0 \int_{-z_0 \operatorname{tg} \theta}^{z_0 \operatorname{tg} \theta} \sqrt{(z_0 \operatorname{tg} \theta)^2 - \xi^2} d\xi \right) \\ &at |x_0 - x_1| > z_0 \operatorname{tg} \theta, |y_0 - y_1| > \sqrt{(z_0 \operatorname{tg} \theta)^2 - (x_0 - x_1)^2}; \\ &= 0 at |x_0 - x_1| > z_0 \operatorname{tg} \theta, |y_0 - y_1| > \sqrt{(z_0 \operatorname{tg} \theta)^2 - (x_0 - x_1)^2}, \end{aligned} \right. \quad (11)$$

describing all the points inside the double light cone in Fig. 2 is introduced in (9) instead of the integration limits and multipliers before the integral of z . The integration with δ -function is performed by changing the order of integration and replacing the variables $\tilde{x}_1 = x_1(z_0 - z)/z_0$, $\tilde{y}_1 = (y_0 - y_1)z/z_0$ in (10) by \tilde{x}_1, \tilde{y}_1 and an equation of the type of two-dimensional convolution by x, y is obtained:

$$\delta I(x_0, y_0, z_0) = \int_0^d dz \iint \mu(x, y, z) F\left[\left(x_0 - x\right) \frac{z_0}{z_0 - z}, \left(y_0 - y\right) \frac{z_0}{z_0 - z}, z_0\right] \left(\frac{z_0}{z_0 - z}\right)^2 dx dy, \quad (12)$$

which by a two-dimensional Fourier transform over x_0 and y_0 reduces to a one-dimensional integral equation in k -space:

$$\delta I(k_x, k_y, z_0) = 4\pi^2 \int_0^d \mu(k_x, k_y, z) K(k_x, k_y, z_0, z) dz, \quad (13)$$

which should be solved for each pair of k_x, k_y components of the spatial spectrum. Then the inverse Fourier transform of the obtained solution $\mu(k_x, k_y, z)$ also gives the solution $\mu(x, y, z)$ of the posed tomography problem in Cartesian coordinates:

$$\mu(x, y, z) = \iint \mu(k_x, k_y, z) \exp(-ik_x x - ik_y y) dk_x dk_y. \quad (14)$$

The kernel of equation (13) can be determined from an experiment with a thin (by z) test object with a known transverse k spectrum using the methodology proposed in [25], for example, a homogeneous parallelepiped with a known absorption coefficient μ_0 :

$$K(k_x, k_y, z_0, z) = \delta I(k_x, k_y, z_0) / 4\pi^2 \mu_0(z) \Delta z. \quad (15)$$

If the integral is taken in the function F in (11), then (12) is reduced to a convolution type equation in all three

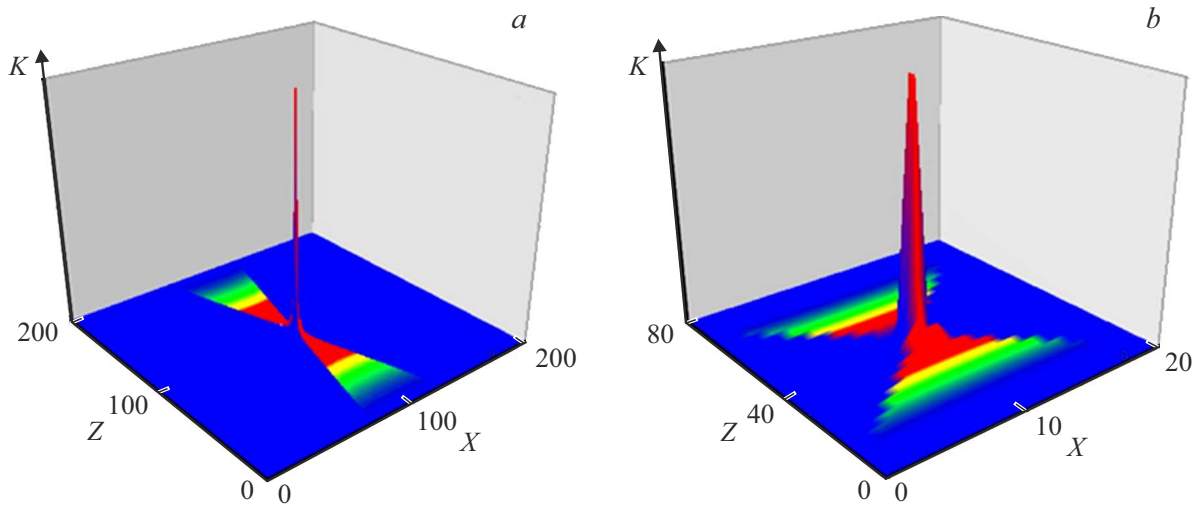


Figure 3. Kernel function (17) of equation (18) $K(x, y, z)$ in section $Y = 0$ at $\theta = 15.65^\circ$: a — sampling $200 \times 200 \times 200$ pixels; b — $20 \times 20 \times 80$ pixels.

coordinates:

$$\delta I(x_0, y_0, z_0) = \int_0^d \iint \mu(x, y, z) K(x_0 - x, y_0 - y, z_0 - z) \times dx dy dz, \tag{16}$$

where

$$K(x_0 - x, y_0 - y, z_0 - z) = \left\{ \begin{aligned} &= \frac{2}{\pi(\operatorname{tg} \theta)^2(z_0 - z)^2} \sqrt{\left(\frac{x_0 - x}{z_0 - z}\right)^2 + \left(\frac{y_0 - y}{z_0 - z}\right)^2 + 1}, \\ &at \left| \frac{x_0 - x}{z_0 - z} \right| < \operatorname{tg} \theta, \left| \frac{y_0 - y}{z_0 - z} \right| < \sqrt{(\operatorname{tg} \theta)^2 - \left(\frac{x_0 - x}{z_0 - z}\right)^2}; \\ &= 0 at \left| \frac{x_0 - x}{z_0 - z} \right| > \operatorname{tg} \theta, \left| \frac{y_0 - y}{z_0 - z} \right| > \sqrt{(\operatorname{tg} \theta)^2 - \left(\frac{x_0 - x}{z_0 - z}\right)^2}. \end{aligned} \right. \tag{17}$$

The three-dimensional Fourier transform leads (18) to a simple equation for spectra in k -space

$$\delta I(k_x, k_y, k_z) = 8\pi^3 \mu(k_x, k_y, k_z) K(k_x, k_y, k_z), \tag{18}$$

and the formula for the desired inverse Radon transform for this tomography method:

$$\mu(x, y, z) = \frac{1}{8\pi^3} \iiint \delta I(k_x, k_y, k_z) / K(k_x, k_y, k_z) \times e^{ik_x x + ik_y y + ik_z z} dk_x dk_y dk_z. \tag{19}$$

It is known that this solution of inverse convolution type problems for input data with an error is an incorrect problem [21]. Random errors can have a wider spatial spectrum than the kernel spectrum, which leads to unlimited

amplification of small-scale components in the solution; in addition, the kernel spectrum can have zeros. Therefore, it is necessary to apply appropriate regularization methods to solve this problem. According to the theory of A.N. Tikhonov [21], the following algorithm can be used to regularize the solution of convolution-type equations:

$$\mu(x, y, z) = \frac{1}{8\pi^3} \iiint \frac{\delta I(-k_x, -k_y, -k_z) K(k_x, k_y, k_z)}{|K(k_x, k_y, k_z)|^2 + \alpha [1 + (k_x^2 + k_y^2 + k_z^2)^2]} \times e^{ik_x x + ik_y y + ik_z z} dk_x dk_y dk_z. \tag{20}$$

The regularization parameter α determines the degree of smoothness of the approximate solution. At large values, the high-frequency (small-scale) components in the reconstructed distribution are suppressed, and small details are smoothed out, with a decrease of α the solution approaches the exact one, but high-frequency data errors increase and details (artifacts) that do not exist in reality appear, starting from a certain level. Such variation by the regularization parameter is somewhat similar to focusing an image with a lens.

Mathematically consistent Tikhonov generalized residual method [21] automatically determines the regularization parameter α from the condition that the residual is equal to the parameter of the total error of the data and the kernel of the equation in the corresponding metrics (Tikhonov generalized residual method), which makes it universally applicable. With this choice, the convergence of the solution to the exact one is proved when the error parameter tends to zero. In reality, the error of the data and the kernel of the equation (due to discretization) cannot be directed to zero, but experience shows that the use of this method with a finite error is the optimal compromise between smoothing the solution and the possibility of artifacts [26]. In contrast to the problems in the correct formulation, the

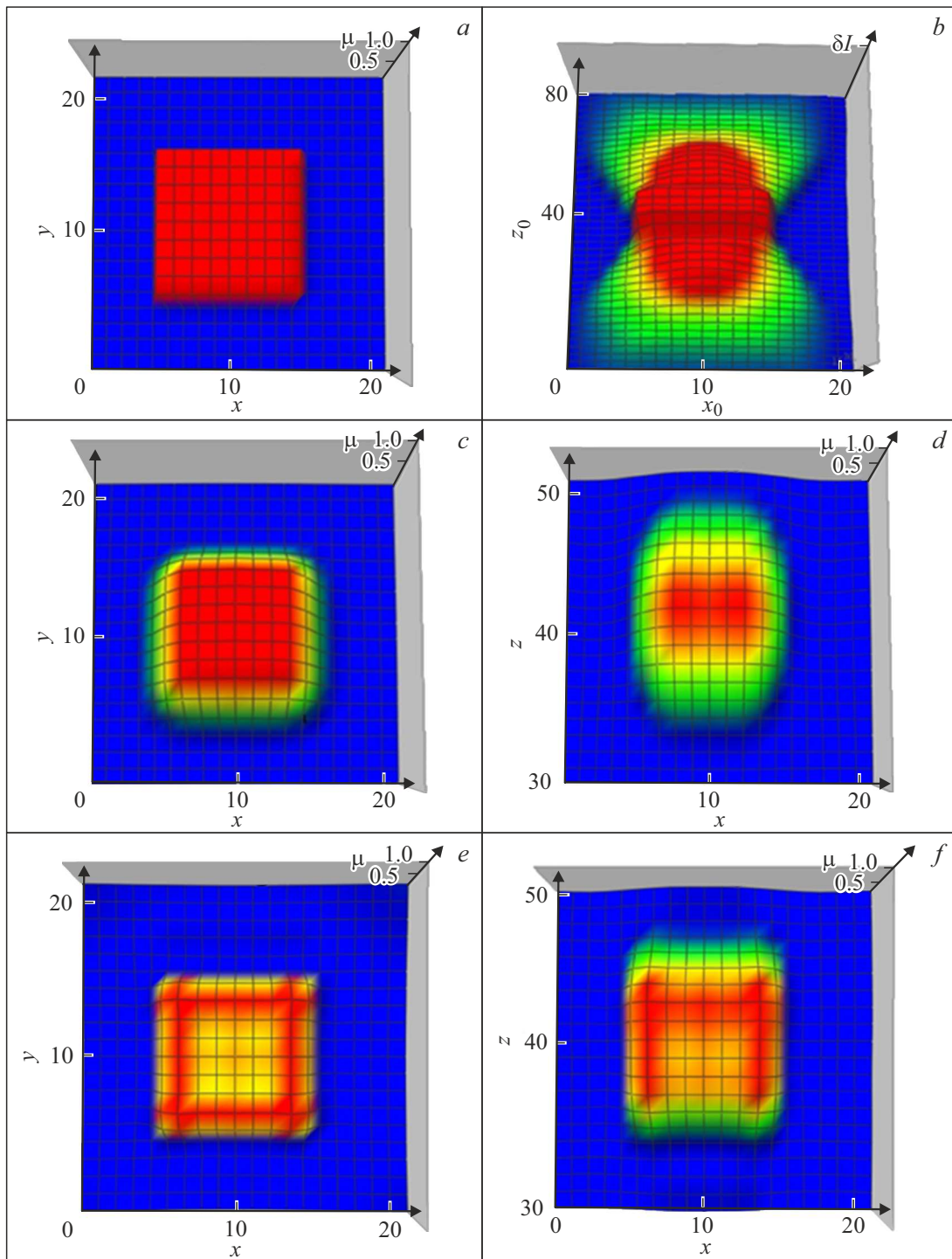


Figure 4. *a* — the initial distribution of the continuous inhomogeneity of the absorption coefficient $\mu(x, y, z)$ in the horizontal section $z = 0$ (in the vertical section, the object is also a square); *b* — distribution „of the measured signal“ $\delta I(x_0, y_0, z_0)$ with added error with standard deviation $\sigma = 5\%$ in vertical section $y_0 = 0$; *c* — restored absorption coefficient distribution $\mu(x, y, z)$ in horizontal section $z = 0$; *d* — reconstructed distribution of the absorption coefficient in the vertical section $y = 0$; *e* — restored with a reduced value of the regularization parameter α absorption coefficient distribution $\mu(x, y, z)$ in horizontal section $z = 0$; *f* — restored with a reduced value α absorption coefficient distribution $\mu(x, y, z)$ in vertical section $y = 0$.

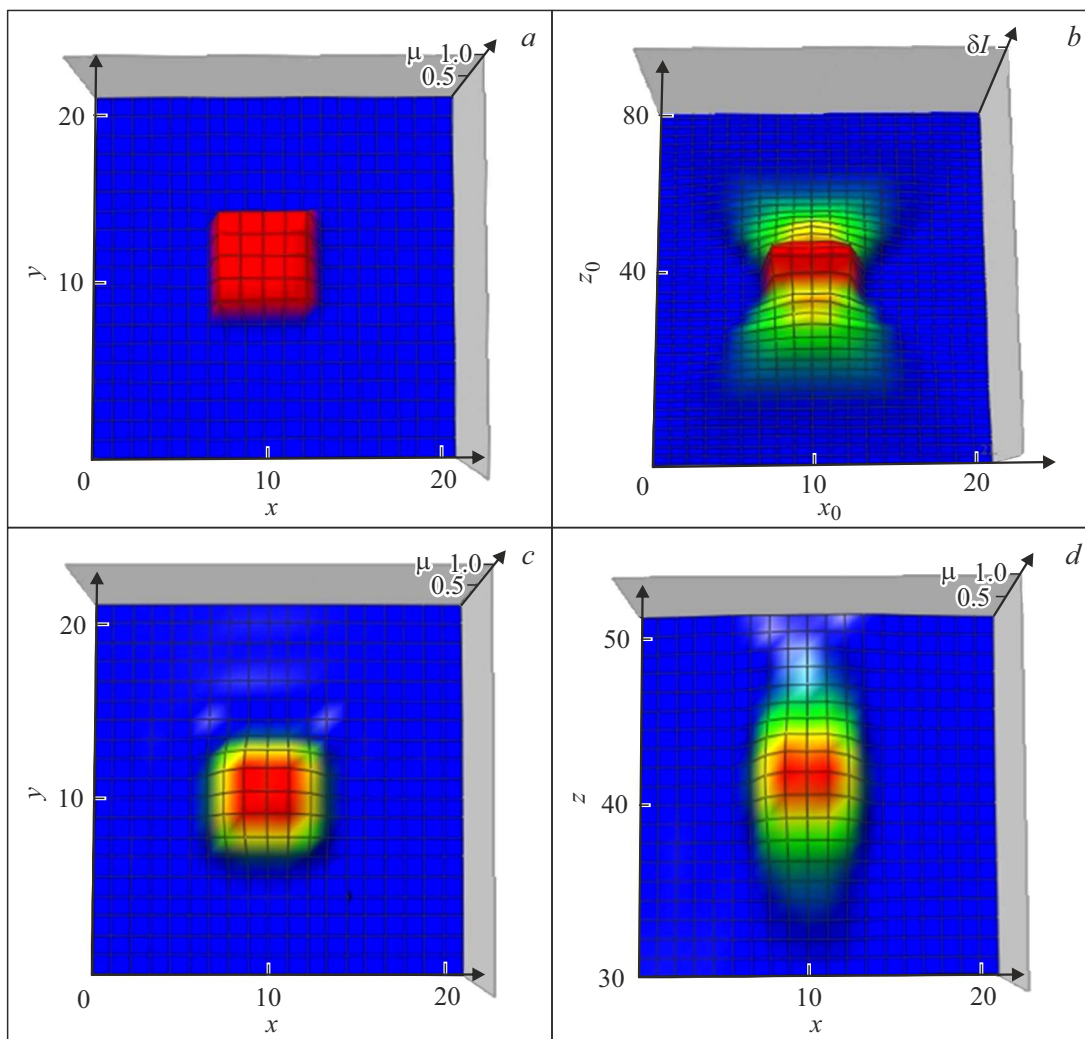


Figure 5. *a* — initial distribution in horizontal section $z = 0$; *b* — signal distribution $\delta I(x_0, y_0, z_0)$ in vertical section $y_0 = 0$; *c* — restored distribution $\mu(x, y, z)$ in horizontal section $z = 0$; *d* — restored distribution $\mu(x, y, z)$ in vertical section $y = 0$.

error of the solution is not proportional to the accuracy of the data, and the convergence to the exact solution is significantly slower — moreover, the accuracy of the solution significantly depends on the complexity of the reconstructed distribution.

An alternative may be to choose α in (20) based on numerical experiment. There is an opportunity to choose a strategy in this case: it is possible to try to avoid artifacts by choosing a sufficiently large value of α , and it is possible to reduce this value by achieving greater contrast and sharpness of the boundaries of the objects being restored (analogies in radar applications — false alarm errors and missing targets, respectively). The method of selecting the value α above the level of appearance of artifacts was used in presented in numerical modeling, due to the relatively large resource intensity of the generalized discrepancy method.

In practical application of the method to the developed measuring system, tomography errors will also include

errors related to diffraction divergence and aberrations due to the residual error in the shape of the lens mirrors [16]. In this case, the diffraction divergence leads to a violation of the difference form of the kernel at the coordinate z . This effect may be insignificant if the divergence is insignificant in the interval of z , in which the inhomogeneity under study is located. In any case, the form of the function K will need to be clarified from (15) in an experiment with a test sample of a known shape. It is necessary to apply a tomography algorithm based on solving equation (12) with the kernel obtained from the experiment if it turns out that errors due to diffraction divergence are significant.

2.3. Numerical simulation

A computer program implementing the algorithm of microscopic tomography (20) was developed and numerical modeling was performed. The simulation scheme included:

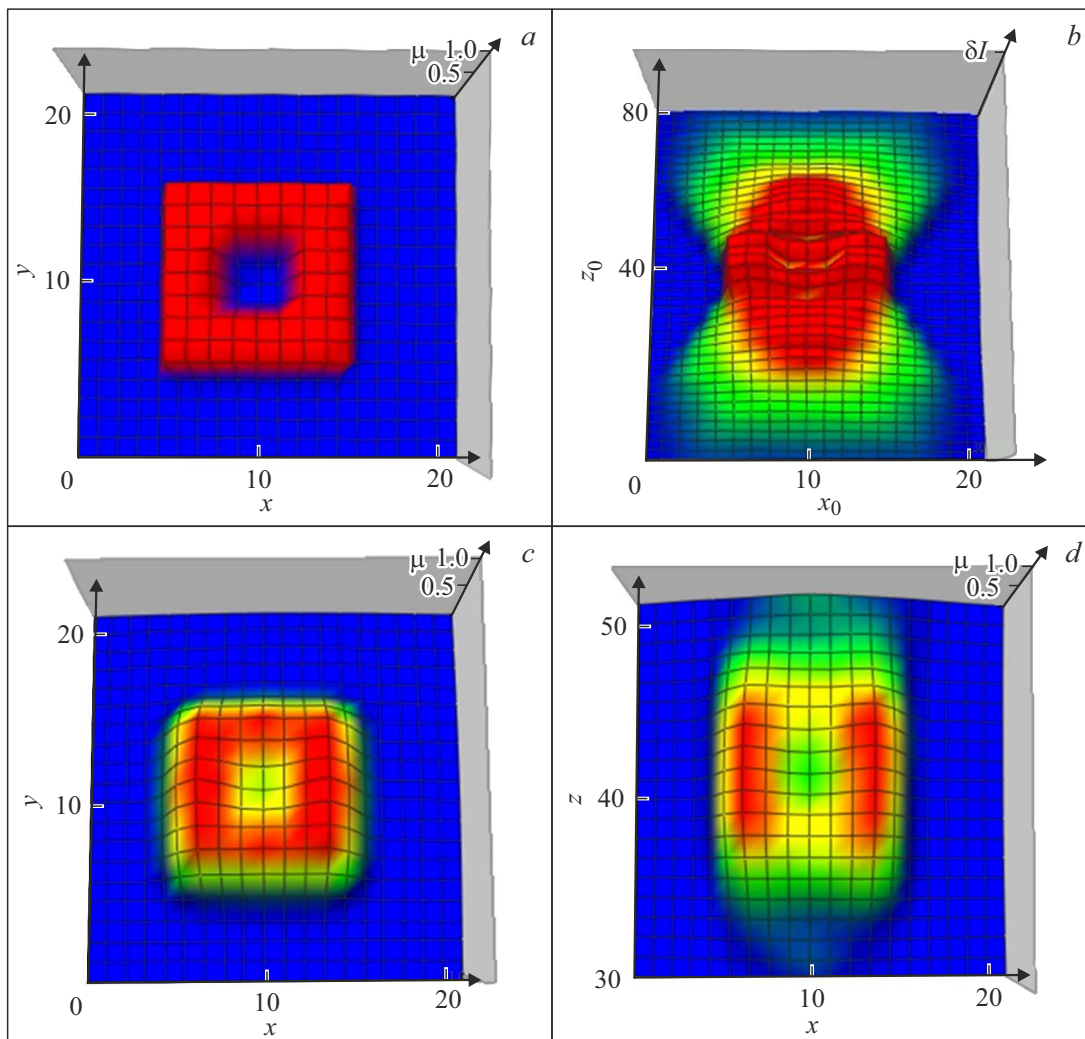


Figure 6. *a* — initial distribution $\mu(x, y, z)$ in horizontal section $z = 0$; *b* — signal distribution $\delta I(x_0, y_0, z_0)$ in vertical section $y_0 = 0$; *c* — reconstructed distribution $\mu(x, y, z)$ in horizontal section $z = 0$; *d* — restored distribution $\mu(x, y, z)$ in vertical section $y = 0$.

a) the distribution of the received signal was calculated depending on the position of the focus in the sensing area for test objects with a given geometric structure (homogeneous in absorption coefficient of parallelepipeds and inhomogeneous, modeled by Gaussian distributions) from (16), (17);

b) „measurement data“ were generated: „measurement error“ with zero mean value and a given level of standard deviation σI was added to the calculated values of the received signal using a random number sensor;

c) the inverse problem for equation (16) was solved using the regularizing algorithm (20), and the resulting solution was compared with the given model distribution;

d) the algorithm parameters were optimized based on modeling: discretization, spatial spectrum of analysis, parameters of the regularization algorithm.

It was possible to use dimensionless coordinates, signal parameters and the absorption coefficient of the probed objects (model distributions with a maximum value of

$\mu = 1$ were used) in the simulation, which ensures the universal applicability of the results obtained. It was assumed that the linear pixel size during the sampling of calculations corresponds to the transverse size of the diffraction spreading of the probing radiation in focus. Since the geometric optics approximation does not describe the intensity distribution on this scale (it increases indefinitely), it was assumed in numerical modeling that the radiation intensity in the focus, which in reality is smoothed out on the scale of the corresponding pixel, does not change between the pixels closest to the focus. It should be noted the value of K in (17) is zero that at the angle $\theta < 45^\circ$ under the conditions of constraints at the focus point. The applicability of this approximation is planned to be investigated experimentally, using the possibility of determining the kernel of the equation to be solved from (15) based on the results of the above measurements with test objects.

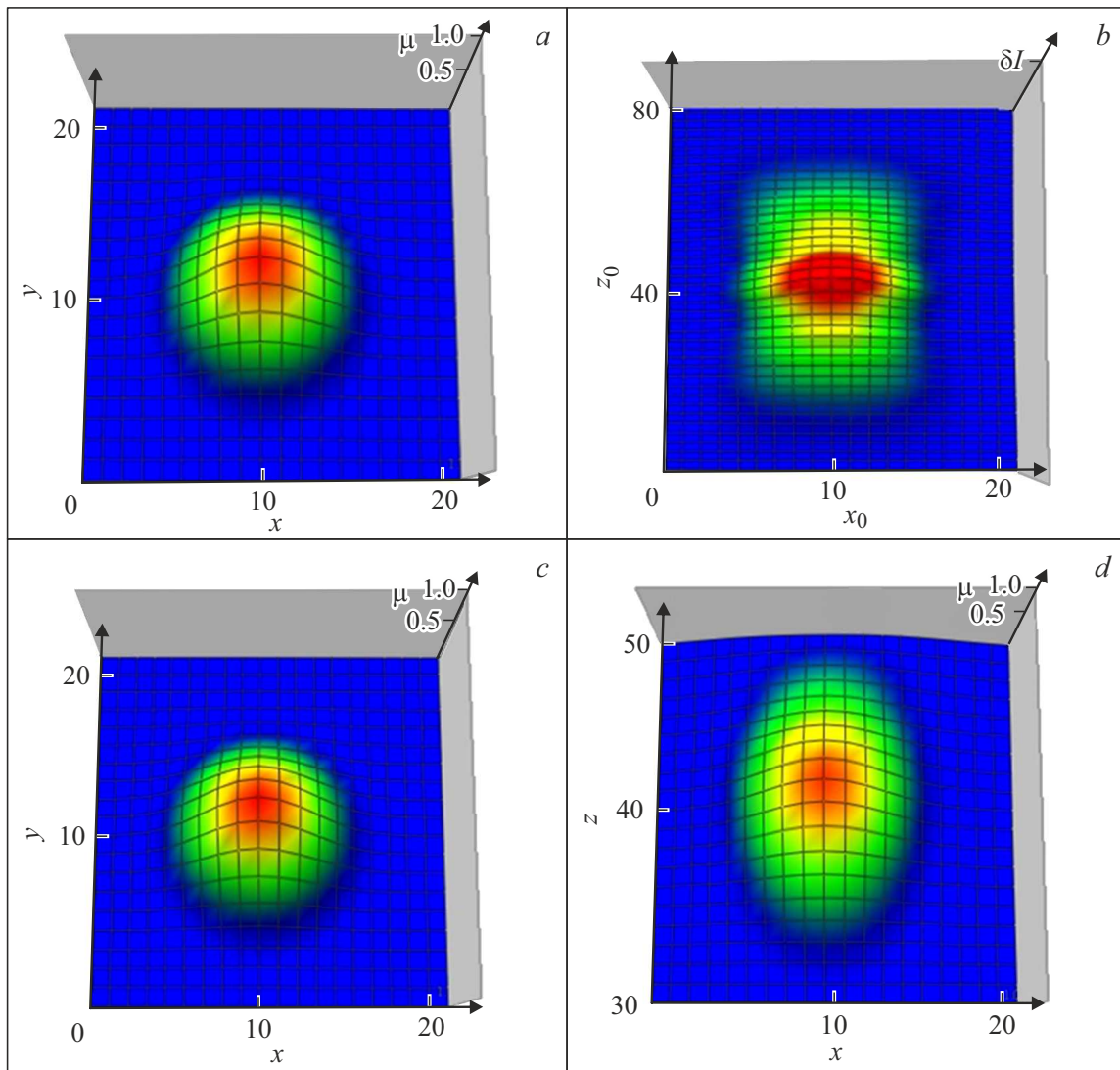


Figure 7. *a* — original distribution $\mu(x, y, z)$ (23) in horizontal section $z = 0$; *b* — signal distribution $\delta I(x_0, y_0, z_0)$ in vertical section $y_0 = 0$; *c* — restored distribution $\mu(x, y, z)$ in horizontal section $z = 0$; *d* — restored distribution $\mu(x, y, z)$ in vertical section $y = 0$.

Numerical analysis assumed calculation and analysis of the kernel integral equation (16). Fig. 3, *a* shows the distribution of this kernel function in the difference coordinates $X = x_0 - x$, $Y = y_0 - y$, $Z = z_0 - z$ at an angle $\theta = 15.65^\circ$ degrees in section $Y = \text{const}$ for 200-pixel sampling by coordinates corresponding to the sampling of data in the developed measuring system, and Fig. 3, *b* shows the distribution K in a narrower area with sampling $20 \times 20 \times 80$ pixels, which was selected in the numerical simulation of small objects to determine the resolution of the computer implementation of the algorithm (22).

The simulation showed that for small objects (inside the 20-pixel volume of the camera), an 80-pixel scan at height z is quite enough. Both solid objects and distributed inhomogeneities of the absorption coefficient were studied. The bandwidth of the analysis by coordinates in k -space was $\Delta j_{x,y,z} = 1.35\pi$.

Figure 4 shows the results of modeling a continuous inhomogeneity in the form of a cube with dimensions $8 \times 8 \times 8$. It was found in numerical modeling that random errors, even with the value of the standard deviation $\sigma = 10\%$ of the calculated signal distribution, do not lead to significant distortions in the reconstructed distributions. The addition of an error with $\sigma = 5\%$ was further used in the considered case. The observed distortions in the form of smoothing the edges of the object are mainly due to the discretization of the problem and the manifestation of its incorrectness. At the same time, the spread of the restored distribution in the vertical plane in Fig. 4, *d* is significantly larger than in the vertical plane in Fig. 4, *c*, which is attributable to the observed in Fig. 4, *b* by the asymmetry of the kernel function of the equation (Fig. 3). Fig. 4, *c* shows a clearly defined area of focus passing through the object, which is close in shape to the observed object.

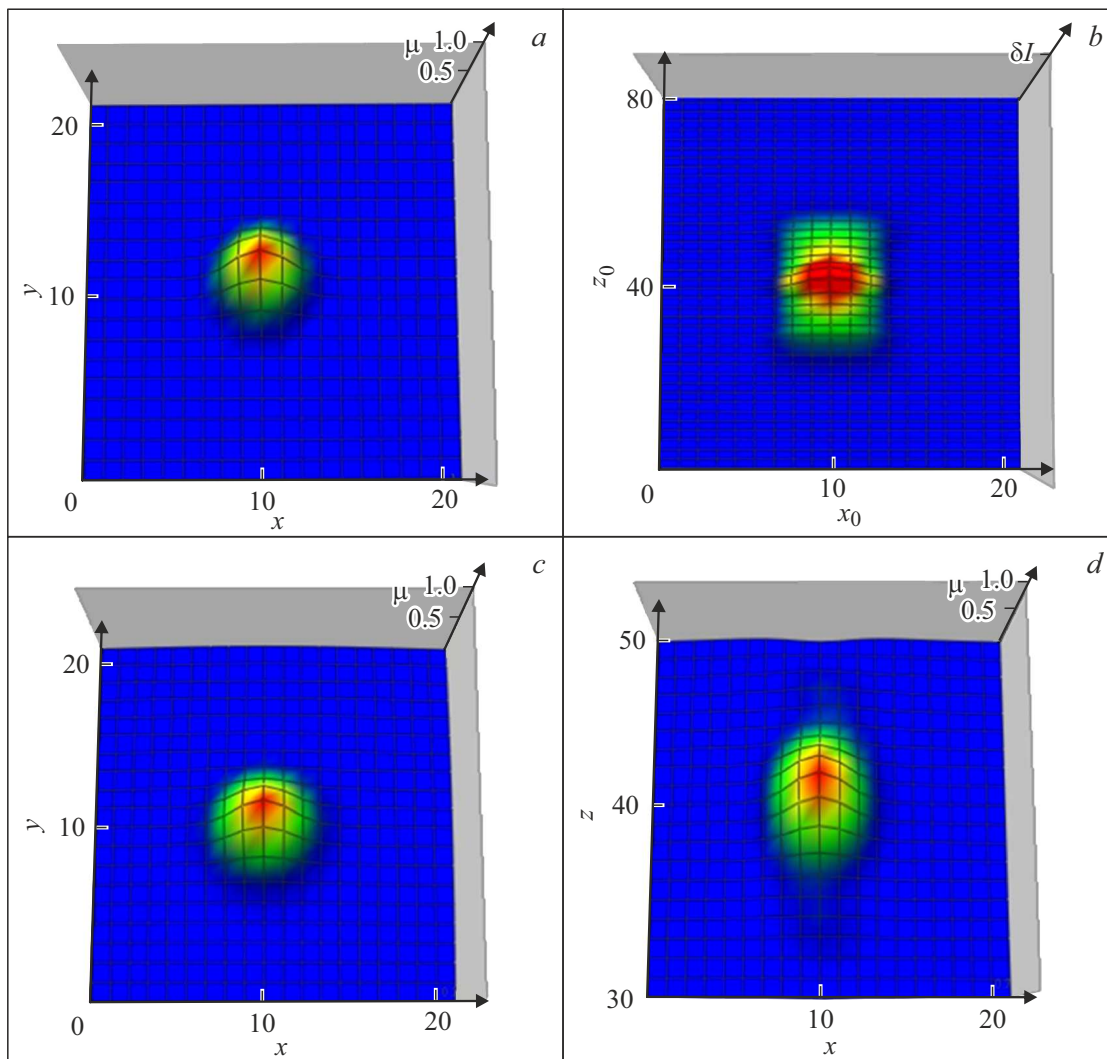


Figure 8. *a* — initial distribution $\mu(x, y, z)$ (23) of the reduced variance in horizontal section $z = 0$; *b* — signal distribution $\delta I(x_0, y_0, z_0)$ in vertical section $y_0 = 0$; *c* — restored distribution $\mu(x, y, z)$ in horizontal section $z = 0$; *d* — restored distribution $\mu(x, y, z)$ in vertical section $y = 0$.

As a consequence, the transverse distribution of the signal in this region practically coincides with the reconstructed distribution of the absorption coefficient shown in Fig. 4, *c*, and therefore is not given hereafter.

The errors in restoring the values of the absorption coefficient in the central part of the restored distributions do not exceed 2–3%. Fig. 4, *e, f* shows the recovery results with a reduced value of the regularization parameter α . It can be seen that other features of the incorrectness of the problem manifest themselves with a decrease in the role of regularization: despite a slight decrease in the blurring of the edges of the object, artifacts — extra details appear, which at the edges manifest themselves as the well-known Gibbs effect.

Figure 5 shows the simulation results for a solid object in the form of a cube with half the linear dimensions $4 \times 4 \times 4$.

It turned out that in this case, too, the shape and magnitude of the simulated inhomogeneity are reproduced almost with the same accuracy as in the case shown in Fig. 4, however, the blurring relative to the linear dimensions of the object increases, and with further reduction of the object it is already reproduced as a blurred spot.

The modeling of such a complex object as a cube with dimensions $8 \times 8 \times 8$ with a cubic cavity with dimensions $4 \times 4 \times 4$ in the center with faces parallel to the corresponding faces of the outer cube was performed since the quality of the solution significantly depends on the degree of complexity of the heterogeneity structure in incorrect problems. Fig. 6 shows the simulation results.

Fig. 6, *c* shows that the object retains a general geometric structure in the central cross-section but with a non-zero absorption coefficient in the cavity. It follows from consideration of the transverse structure of the restored object

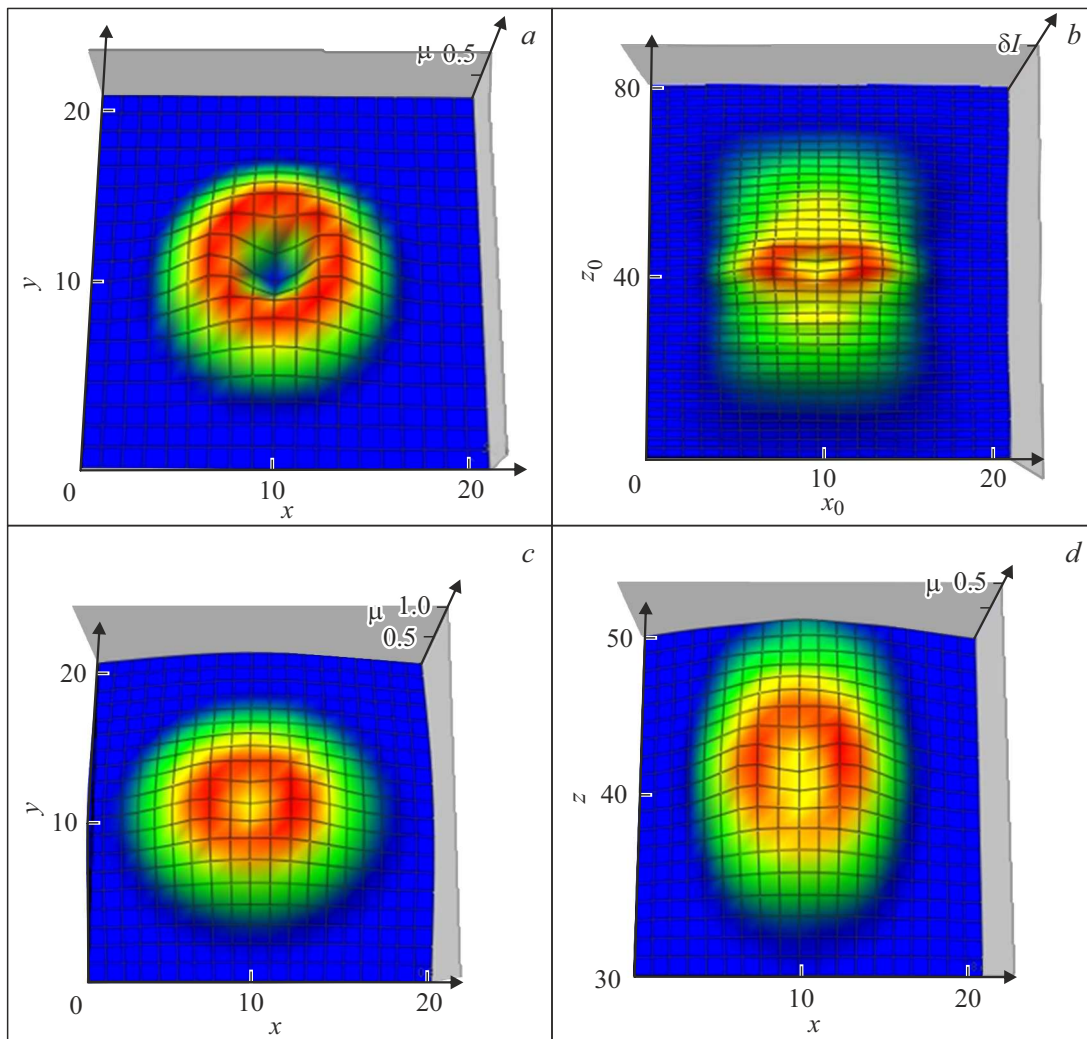


Figure 9. *a* — original distribution $\mu(x, y, z)$ (24) in horizontal section $z = 0$; *b* — signal distribution $\delta I(x_0, y_0, z_0)$ in vertical section $y_0 = 0$; *c* — restored distribution $\mu(x, y, z)$ in horizontal section $z = 0$; *d* — restored distribution $\mu(x, y, z)$ in vertical section $y = 0$.

in Fig. 6, *d* that this structure blurs as the distance from the center increases, and beyond the actual size of the object merges and gradually disappears with a characteristic scale of three to four pixels.

Tomography modeling of distributed inhomogeneities based on 3D Gaussian distributions of the absorption coefficient was also performed. Figure 7 shows the results for the structure described by the formula

$$\mu(x, y, z) = \exp \left[-\frac{(x - x_c)^2}{\sigma_x^2} - \frac{(y - y_c)^2}{\sigma_y^2} - \frac{(z - z_c)^2}{\sigma_z^2} \right], \tag{21}$$

where $x_c = 10, y_c = 10, z_c = 40, \sigma_x = \sigma_y = \sigma_z = 4$.

The comparison of Fig. 7, *a* and *b* shows that the distribution of the refractive index is restored almost exactly in the central section, but as shown on Fig. 7, *d*, it spreads out significantly in the vertical direction.

Figure 8 shows the simulation results for a narrower Gaussian inhomogeneity (21) at $\sigma_x = \sigma_y = \sigma_z = 2$.

The quality of the reconstruction of a narrower Gaussian inhomogeneity turned out to be no worse than that shown in Fig. 7, however, data sampling turns out to be insufficient for a satisfactory solution of the problem with a further decrease in the variance.

A modeling was performed for more complex, non-simply connected inhomogeneities like in case of continuous inhomogeneities, based on combinations of two 3D Gaussian distributions:

$$\begin{aligned} \mu(x, y, z) = & a_1 \exp \left[-\frac{(x - x_{c1})^2}{\sigma_{x1}^2} - \frac{(y - y_{c1})^2}{\sigma_{y1}^2} - \frac{(z - z_{c1})^2}{\sigma_{z1}^2} \right] \\ & + a_2 \exp \left[-\frac{(x - x_{c2})^2}{\sigma_{x2}^2} - \frac{(y - y_{c2})^2}{\sigma_{y2}^2} - \frac{(z - z_{c2})^2}{\sigma_{z2}^2} \right]. \end{aligned} \tag{22}$$

Figure 9 shows simulations for Gaussian inhomogeneity (22) with parameters $a_1 = 1, a_2 = -1, \sigma_{x1} = \sigma_{y1} = \sigma_{z1} = 4, \sigma_{x2} = \sigma_{y2} = \sigma_{z2} = 2, x_{c1} = x_{c2} = 10,$

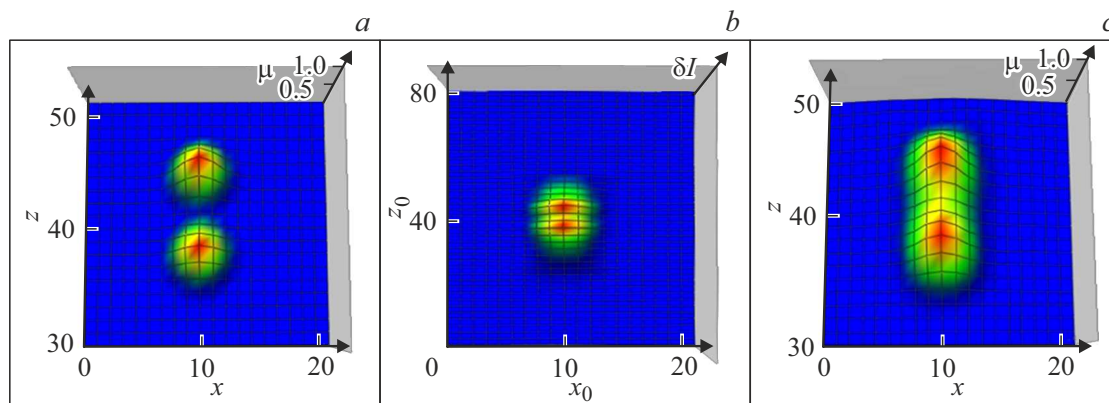


Figure 10. *a* — initial distribution $\mu(x, y, z)$ (24) in vertical section $y = 0$; *b* — signal distribution $\delta I(x_0, y_0, z_0)$ in vertical section $y_0 = 0$; *c* — restored distribution $\mu(x, y, z)$ in the vertical section $y = 0$.

$y_{c1} = y_{c2} = 10$, $z_{c1} = z_{c2} = 40$. This distribution forms a structure with a cavity filling from the center to the edges.

Fig. 9, *c, d* shows that the reconstructed distributions also reproduce the cavity and the original inhomogeneities in Fig. 9, *a*, but near the center it blurs and does not reach values close to zero.

The minimum distance at which it is possible to reconstruct narrow Gaussian inhomogeneities spaced along the vertical coordinate, shown in Fig. 10. It turned out that this distance is 6 pixels between their centers. The corresponding total distribution of the absorption coefficient is described by the formula (22) with the parameters $a_1 = 1$, $a_2 = 1$, $\sigma_{x1} = \sigma_{y1} = \sigma_{z1} = \sigma_{x2} = \sigma_{y2} = \sigma_{z2} = 2$, $x_{c1} = x_{c2} = 10$, $y_{c1} = y_{c2} = 10$, $z_{c1} = 37$, $z_{c2} = 43$.

Fig. 10, *c* shows that the blurring of the restored inhomogeneities leads to their overlap. The inhomogeneities merge and become indistinguishable with a smaller separation along the vertical coordinate.

Conclusion

The above simulation results of direct and reconstructed three-dimensional images confirm the operability and sufficient effectiveness of the developed algorithm of axial X-ray tomography in high-aperture soft X-ray microscopy. The algorithm can be refined to practical application on the basis of experimental refinement of the kernel function of equation (16) or modification based on the use of equation (12) in case diffraction blurring disturbs the difference form of the equation along the vertical coordinate.

Funding

The study was supported by a grant from the Russian Science Foundation (Project №22-62-00068).

Conflict of interest

The authors declare that they have no conflict of interest.

References

- [1] E. Hanssen, C. Knoechel, M. Dearnley, M.W.A. Dixon, M. Le Gros, C. Larabel, L. Tilley. *J. Structural Biol.*, **177**, 224 (2012).
- [2] D. Sage, L. Donati, F. Soulez, D. Fortun, G. Schmit, A. Seitz, R. Guiet, C. Vonesch, M. Unser. *Methods*, **115**, 28 (2017).
- [3] G. Vicidomini, P. Bianchini, A. Diaspro. *Nat. Methods*, **15**, 173 (2018).
- [4] V. Lučić, A. Rigort, W. Baumeister. *J. Cell Biol.*, **202** (3), 407 (2013).
- [5] K.E. Leigh, P.P. Navarro, S. Scaramuzza, W. Chen, Y. Zhang, D. Castaño-Diez, M. Kudryashev. *Methods Cell Biol.*, **152**, 217 (2019). DOI: 10.1016/bs.mcb.2019.04.003
- [6] P.A.C. Takman, H. Stollberg, G.A. Johansson, A. Holmberg, M. Lindblom, H.M. Hertz. *J. Microscopy*, **226**, 175 (2007).
- [7] C.A. Larabell, M.A. Le Gros. *Molecular Biol. Cell*, **15**, 957 (2004).
- [8] D. Weib, G. Schneider, B. Niemann, P. Guttmann, D. Rudolph, G. Schmah. *Ultramicroscopy*, **84**, 185 (2000).
- [9] M. Bertilson, O. von Hofsten, U. Vogt, A. Holmberg, E. Athanasia, Christakou, H.M. Hertz. *Opt. Lett.*, **36** (14), 2728 (2011).
- [10] M. Bertilson, O. von Hofsten, U. Vogt, A. Holmberg, H.M. Hertz. *Opt. Expr.*, **17** (13), 11057 (2009).
- [11] M. Toyoda, K. Yamasoe, T. Hatano, M. Yanagihara, A. Tokimasa, T. Harada, T. Watanabe, H. Kinoshita. *Appl. Phys. Express.*, **5** (11), 112501 (2012).
- [12] L. Juschkín, R. Freiburger, K. Bergmann. *J. Phys.: Conf. Ser.*, **186**, 012030 (2009).
- [13] A. Torrisi, P. Wachulak, Ł. Wegrzyn'ski, T. Fok, A. Bartnik, T. Parkman, Š. Vondrová, J. Turňová, B.J. Jankiewicz, B. Bartosewicz, H. Fiedorowicz. *J. Microscopy*, **00** (0), 1 (2016). DOI: 10.1111/jmi.12494
- [14] P.W. Wachulak, A. Torrisi, A. Bartnik, Ł. Wegrzyn'ski, T. Fok, H. Fiedorowicz. *Appl. Phys. B*, **123**, 25 (2017).
- [15] T. Ejima, F. Ishida, H. Murata, M. Toyoda, T. Harada, T. Tsuru, T. Hatano, M. Yanagihara, M. Yamamoto, H. Mizutani. *Opt. Express*, **18** (7), 7203 (2010).
- [16] I.V. Malyshev, D.G. Reunov, N.I. Chkhalo. *Opt. Expr.*, **30** (26), 47567 (2022). DOI: 10.1364/OE.475032

- [17] A.V. Vodop'yanov, S.A. Garakhin, I.G. Zabrodin, S.Yu. Zuev, A.Ya. Lopatin, A.N. Nechay, A.E. Pestov, A.A. Perekalov, R.S. Pleshkov, V.N. Polkovnikov. *Quantum Electronics*, **51** (8), 700 (2021).
- [18] I.V. Malyshev, A.E. Pestov, V.N. Polkovnikov, N.N. Salashchenko, M.N. Toporov, N.I. Chkhalo. *Poverkhnost: rentgenovskie, sinkhrotronnye i neytronnye issledovaniya*, **1**, 3 (2019).
- [19] N.I. Chkhalo, M.N. Drozdov, E.B. Kluev, S.V. Kuzin, A.Ya. Lopatin, V.I. Luchin, N.N. Salashchenko, N.N. Tsybin, S.Yu. Zuev. *Appl. Optics*, **55** (17), 4683 (2016).
- [20] J. Radon. *Akad. Wiss.*, **69**, 262 (1917)
- [21] A.N. Tikhonov, V.Ya. Arsenin. *Metody resheniya nekorrektnykh zadach* (Nauka, M., 1986) (in Russian).
- [22] A.N. Tikhonov, V.Ya. Arsenin, A.A. Timonov. *Matematicheskie zadachi komp'yuternoj tomografii* (Nauka, M., 1987) (in Russian).
- [23] A.N. Tikhonov, A.V. Goncharsky, I.V. Kochikov, E.I. Rau, D.O. Savin, G.V. Spivakov, V.V. Stepanov. *Dokl. AN SSSR*, **289** (5), 1104 (1986) (in Russian).
- [24] A.N. Tikhonov, P.N. Bochikashvili, A.V. Goncharsky, A.N. Matvienko, E.I. Rau, D.O. Savin, V.V. Stepanov. *Dokl. AN SSSR*, **296** (5), 1095 (1987) (in Russian).
- [25] K.P. Gaikovich, P.K. Gaikovich, Ye.S. Maksimovitch, V.A. Badeev. *Phys. Rev. Lett.*, **108** (16), 163902 (2012).
- [26] K.P. Gaikovich. *Inverse Problems in Physical Diagnostics* (Nova Science Publishers Inc., NY., 2004)

Translated by A.Akhtyamov